

A novel approach for deriving river discharge using passive microwaves

Yoon Hae Na¹, Marshall Lucy Amanda¹, Sharma Ashish¹, and Kim Seokhyeon²

¹University of New South Wales

²Kyung Hee University

November 16, 2022

Abstract

We present herein a new basis for measuring river discharge in ungauged catchments. Surrogate runoff (SR) is created using remotely sensed data to compensate for the absence of ground streamflow measurements. Because of their widespread availability, remotely sensed SR products are attractive, with approaches such as satellite-derived measurement-calibration ratio (C/M ratio). However, the use of the C/M ratio suffers from its limited penetration through ground vegetation canopies. While a microwave signal with a longer wavelength has been used to enhance the penetration capability, the coarseness of the spatial resolution of the microwave signal offsets its improvement due to the inherent assumptions in the C/M ratio, i.e., selecting two contrasting pixels (i.e., measurement and calibration) at the same time. To address both issues, this study proposes a new SR formulation using a longer wavelength (L-band microwave) with a better assumption for handling coarse grids, whereby the temporal variability of dryness against the driest state in each grid is used. The performance of the new SR is assessed for 467 Australian Hydrologic Reference Station catchments. Results show considerable improvements in the Pearson linear correlation (R) between the proposed SR and streamflow: 44% of the study areas show R higher than 0.4 with the new approach, whereas only 13% of the study areas show R higher than 0.4 with the currently used alternative (C/M ratio derived from Ka-band microwave). Overall, the resulting SR is dramatically improved by using the newly designed SR approach with the L-band microwave signal.

Hosted file

essoar.10512498.1.docx available at <https://authorea.com/users/523796/articles/595320-a-novel-approach-for-deriving-river-discharge-using-passive-microwaves>

Hosted file

si_hnywrr2_sub.docx available at <https://authorea.com/users/523796/articles/595320-a-novel-approach-for-deriving-river-discharge-using-passive-microwaves>

Hae Na Yoon¹, Lucy Marshall¹, Ashish Sharma¹, and Seokhyeon Kim²

¹School of Civil and Environmental Engineering, University of New South Wales, Sydney, New South Wales, Australia

²Department of Civil Engineering, Kyung Hee University, 1732 Deogyong-daero, Giheung-gu, Yongin-si 17104, Republic of Korea

Corresponding author: Lucy Marshall (lucy.marshall@unsw.edu.au)

Key Points:

- A new method is proposed to improve surrogate runoff signals using passive microwaves.
- Eliminating the ambiguity of selecting a calibration pixel in space enables adopting a longer wavelength microwave.
- The new algorithm outperforms existing alternatives in densely forested areas.

Abstract

We present herein a new basis for measuring river discharge in ungauged catchments. Surrogate runoff (SR) is created using remotely sensed data to compensate for the absence of ground streamflow measurements. Because of their widespread availability, remotely sensed SR products are attractive, with approaches such as satellite-derived measurement-calibration ratio (C/M ratio). However, the use of the C/M ratio suffers from its limited penetration through ground vegetation canopies. While a microwave signal with a longer wavelength has been used to enhance the penetration capability, the coarseness of the spatial resolution of the microwave signal offsets its improvement due to the inherent assumptions in the C/M ratio, i.e., selecting two contrasting pixels (i.e., measurement and calibration) at the same time. To address both issues, this study proposes a new SR formulation using a longer wavelength (L-band microwave) with a better assumption for handling coarse grids, whereby the temporal variability of dryness against the driest state in each grid is used. The performance of the new SR is assessed for 467 Australian Hydrologic Reference Station catchments. Results show considerable improvements in the Pearson linear correlation (R) between the proposed SR and streamflow: 44% of the study areas show R higher than 0.4 with the new approach, whereas only 13% of the study areas show R higher than 0.4 with the currently used alternative (C/M ratio derived from Ka-band microwave). Overall, the resulting SR is dramatically improved by using the newly designed SR approach with the L-band microwave signal.

Plain Language Summary

We present a new Surrogate Runoff (SR) that can be used as an alternative to in-situ river discharge, which has limited gauges worldwide. The new measurement is retrieved from satellite data with global coverage for ungauged areas.

Existing SRs are limited due to their limited penetration through ground vegetation canopies. Therefore, a microwave signal with a longer wavelength is an attractive approach because it provides greater penetration and improves the signal's quality. Still, deriving a useful SR product is difficult due to the coarseness of the signal. The new SR formulation is proposed to use a longer wavelength (L-band microwave) by addressing key limitations in a coarse grid. The performance of the new SR is assessed for 467 Australian Hydrologic Reference Station catchments. Results show considerable improvements in accuracy as measured by correlation between the SR and observed streamflow. Overall, the resulting SR is dramatically improved by using the newly designed SR approach with the L-band microwave signal.

1. Introduction

Floods and droughts arguably represent the biggest and most severe natural disasters society faces year after year (Thomas and López, 2015). A key reason for their damaging impact is the lack of a reliable streamflow monitoring network, resulting in poor acceptance of the forecasts by the community (Smith et al., 2019; Tellman et al., 2021). Therefore, measuring hydroclimatic fluxes from space has long been an active area of research, with unprecedented recent opportunities created for measuring water and energy fluxes at the Earth's surface.

Recent studies have added to remote sensing capabilities by creating novel means of assessing flood inundation (Brakenridge and Anderson, 2006; Parinussa et al., 2016) to improve flood forecasts in ungauged catchments. Spatial comparisons of temperature retrievals represent a key remote-sensing measurement pathway, the hypothesis being that lower brightness temperature is synonymous with a greater wetted perimeter (Kim and Sharma, 2019) compared to the drier pixels (the reference pixels) in the image. This has led to the rationale of Surrogate Runoff (SR), also known as the measurement-calibration ratio (C/M ratio or MC ratio; Brakenridge et al., 2007; Brakenridge et al., 2012), representing the ratio of the target temperature and assumed to equal land temperature within the measurement pixel. Using this rationale, the derived SR has been demonstrated to have a high correlation to river discharge (De Groeve, 2010; Brakenridge et al., 2012). While there now exist alternatives to better calibrate hydrologic models using a suitable SR (Yoon et al., 2022), allowing extended streamflow estimates at ungauged catchments worldwide, their efficacy is dependent on the quality of the signal the SR is able to impart. Hence, an advanced surrogate derived from satellite signals is needed to improve hydrologic prediction.

Specifically, there still are limitations in existing SR due to the inherent errors in the observation and necessary assumptions. This assumption becomes critical when longer wavelength electromagnetic waves are used, such as microwaves with greater penetrative capability through the atmosphere and vegetation canopy but operate over a coarse resolution. In contrast, the use of shorter electromagnetic waves covering finer spatial resolutions allows a reference pixel to be assumed as the land reflectance at the measurement pixel but

provides reduced ground penetration (Hou et al. 2020). Whether to use a more precise but longer electromagnetic wave or a less precise but higher resolution shorter electromagnetic wave then depends on how well the reference pixel is specified, a requirement we seek to eliminate in the research proposed here.

In this context, we present here a radically new basis for measuring river discharge using a longer electromagnetic wave, such as the L-band microwave. The end outcome is a robust and reliable framework to create a new surrogate data source that can be implemented in any region regardless of the availability of ground measurements.

The paper is organized as follows. Section 2 introduces the background of previous studies on SRs and compare their strength and weakness. Section 3 develops the new SR from this initial analysis to offer an advanced runoff prediction. Section 4 introduces the study area and data, section 5 illustrates results, section 6 discusses key points, and section 7 summarizes and concludes the main findings.

2. Background

A substantial amount of work is aimed at estimating river discharge using remote sensing data. Early studies used river water levels detected from satellite altimetry data to measure river discharge with Manning’s equation, however, this is generally only possible for the world’s largest rivers (Birkinshaw et al., 2010). Thus, alternative methods have been developed to measure river width or inundation extent to estimate river discharge using radar or optical images (Smith et al., 1996; Smith, 1997). From the assumption that the water inundation is correlated to the river discharge amount (Vörösmarty et al., 1996), several studies then related river discharge to the inundation extent (Bjerklie et al., 2005; Brakenridge et al., 2005; Brakenridge et al., 2012; Papa et al., 2008; Smith and Pavelsky, 2008; Gleason et al., 2014; Pavelsky, 2014; Van Dijk et al., 2016).

From these studies, Brakenridge et al. (2007) developed the brightness temperature ratio, and further studies (see Table 1) improved SR in several aspects, including the source of signal, measurement (M) pixel selection methods, and calibration (C) pixel selection methods. These methods are summarized in Table 1, with the factors that affect the quality of the derived SR. The performance of SR is calculated via the Pearson linear correlation (R) with gauged streamflow. To examine and advance these approaches, we examine three factors affecting the quality of the SR (SR formulations, measurement and calibration cell selection, and wavelength). Then we present the new SR designed to address the limitations of previous SRs.

Table 1 Summary of previous studies on SRs. These are categorized with the SR formulation, the signal source, and the calibration and measurement pixel selection methods (discussed in sections 2.1 ~ 2.4). The definition and detailed information of SR1 and SR2 are described

in section 2.1. In C and M pixel selection, ‘best cells’ refers to cells selected based on their performance, such as a correlation to river discharge. Additionally, ‘Low CV’ means that cells with low coefficients of variance are selected, and ‘Low Tb’ means that cells with low brightness temperature are selected. SD denotes standard deviation. ‘TWI filtering’ denotes the Topographic Wetness Index filtering approach suggested in Kim and Sharma (2019).

SR formation	Signal	C pixel selection	M pixel selection	Reference Study Area	Performance (R)	Temporal resolution
SR1	Ka-band Microwave	Best cells	Single cell	Brakenridges et al., 2007 (USA)	-0.74	Daily
			Single cell	Brakenridges et al., 2012 (USA)	-	
			Single cell	Khan et al., 2014 (Indus River Basin at Pakistan)	-0.84	
			nearest cells	Revilla-Romero et al., 2014 (across the world except Oceania)	-0.4 (42%); 0.4-0.5 (15%); 0.5-1.0 (10%)	
			Best cells	Revilla-Romero et al., 2015 (across the world)	-1.0	
			Best cells	Van Dijk et al., 2016 (across the world)		Monthly

SR formation	Signal	C pixel selection	M pixel selection	Reference	Study Area	Performance (R)	Temporal resolution
			TWI filtering	Kim and Sharma, 2019	Yoon et al., 2021		Daily
		Best cell	Best cells	Kugler et al., 2019	sites (Amazon)	-0.69	
	L-band Microwave	Best cell	Best cells		sites (Amazon)	-0.92	
	Near Infrared	Best cell	Best cells	Tarpanelli et al., 2013	5 sites (Po Tarpanelli river Basin at Italy)	-0.81	
		Reference Area	Inundated area	Li et al., 2019	sites (Heigh River Basin at China)	-0.83	
		Best cell	Single cell	Sahoo et al., 2020	sites (Brahmani River Basin in India)	-0.84	
		Low CV	Best cells	Shi et al., 2020	sites (Murray Darling Basin in Australia)	-0.9	

SR formation	Signal	C pixel selection	M pixel selection	Reference	Study Area	Performance (R)	Temporal resolution
SR2	SWIR (short-wave infrared)	Low Tb	Best cells	Van Dijk et al., 2016	sites (across the world)	–	Monthly
				Hou et al., 2020	sites (across the world)	(30%)	

2.1 SR formulations

Here the SR suggested in Brakenridge et al. (2007) (advocating the use of measurement-calibration ratio) is defined as SR1 to distinguish it from the other SR formulations presented later. As mentioned, SR1 is derived from the brightness temperature of two pixels: the measurement pixel (located on the wetland) and the calibration pixel (located on the dryland). Since the raw brightness temperatures ($T_{b,m}$) are influenced by various local factors such as physical temperature, permittivity, surface roughness, vegetation, atmospheric moisture, and other environmental variables (Brakenridge et al., 2007; Van Dijk et al., 2016), it is scaled by the signal of land observation ($T_{b,c}$). The SR1 derivation starts from the assumption that $T_{b,m}$ exhibits a mixture of a brightness temperature of land ($T_{b,l}$) and water ($T_{b,w}$) in the pixel, allowing the proportion occupied by water (denoted w 0 to 1) to serve as a measure of the stream extent and hence streamflow (Brakenridge et al., 2007; Kugler and De Groeve, 2007), as shown in Equation 1:

$$T_{b,m} = T_m \varepsilon_m = w T_{b,w} + (1 - w) T_{b,l} = T_w (w \varepsilon_w) + T_l (1 - w) \varepsilon_l \quad (1)$$

Following this, the brightness temperature of the calibration pixel is explained as

$$T_{b,c} = T_c \varepsilon_c \quad (2)$$

Here, T_m and T_c are the physical temperatures of the measurement and calibration pixels, and T_w and T_l are the physical temperatures of the water and land area in the calibration pixels, respectively. Additionally, ε_m and ε_c are the emissivity of the measurement and calibration pixels, and ε_w and ε_l are the emissivity of the water and land in the measurement pixels. Here two assumptions are made that ε_c can be estimated with ε_l , and the surface physical temperature T are homogeneous (T_w and T_l are equal to T_m) as:

$$\text{Assumption 1: } \varepsilon_l \approx \varepsilon_c \quad (3)$$

Assumption 2: $T_m \approx T_c \approx T_w$. (4)

Then, the inverse of SR1 can be written as:

$$\frac{T_{b,m}}{T_{b,c}} = \frac{T_m(w\varepsilon_w + (1-w)\varepsilon_l)}{T_c\varepsilon_c} \approx 1 - w + w\frac{\varepsilon_w}{\varepsilon_l} = 1 - w(1 - \frac{\varepsilon_w}{\varepsilon_l}) = f(w) \quad ()$$

The inverse of $f(w)$, $g(w)$, is known to be correlated to streamflow (De Groeve, 2010); resulting in SR1 being defined as

$$\text{SR1} := \frac{T_{b,c}}{T_{b,m}} = g(w) = 1/f(w) \quad ()$$

Here, it is required that the value of $1 - \frac{\varepsilon_w}{\varepsilon_l}$ is a constant or a variant proportional to w to ensure that $g(w)$ is an increasing function of w . Thus, there is a hidden assumption in SR1 as

Assumption 3: $1 - \frac{\varepsilon_w}{\varepsilon_l} \propto w$ or $1 - \frac{\varepsilon_w}{\varepsilon_l} \approx \text{constant}$. ()

However, this assumption may not be valid in some conditions since ε_l can be affected by w , based on the relationship between the ε_l and soil moisture (Schmugge, 1983; Owe and Van De Griend, 1998) relative to the surface water extent (Ghajarnia et al., 2020).

Thereafter, Van Dijk et al. (2016) developed an alternative from the same linear mixing model in De Groeve (2010), which is expressed as,

$$\varepsilon_m = w\varepsilon_w + (1 - w)\varepsilon_l \quad (8)$$

following which SR2 is derived as an estimate of w via:

$$r = 1 - \varepsilon \quad (9)$$

$$w = \frac{r_m - r_l}{r_w - r_l} \quad (10)$$

where r is reflectance and ε is emissivity that satisfies Equation 9, r_m is the reflectance of the measurement pixel, r_l is the reflectance of the land in that measurement cell, and r_w is the reflectance of the water extent. Then, r_l is inferred from the reflectance of the calibration cell (r_c) with Assumption 1 (Equation 4), and this results in SR2 being

$$\text{SR2} := \frac{r_m - r_c}{r_w - r_c} \quad (11)$$

Here, the use of reflectance instead of brightness temperature eliminates two assumptions (Assumption 2 and 3), which amplifies the uncertainty of SR1. The reflectance of the water is considered constant in both SRs, although it is not truly constant because r_w has a low variability (Hou et al., 2020).

2.2 Selecting measurement and calibration cells

In deriving SR, a measurement pixel must be carefully selected to make a proper prediction. Although the high performance of the pixel selection is based on their metrics, such as the correlation to streamflow (Brakenridge et al., 2007; Brakenridge et al., 2012; Khan et al., 2014; Kugler et al., 2019; Tarpanelli

et al., 2013; Tarpanelli et al., 2017), it requires the information of the in-situ water discharge data. Therefore, other approaches were developed to collect measurement cells. Revilla-Romero et al. (2014) proposed spatially averaging over the three nearest neighbors of the grid where a gauge exists. Additionally, Kim and Sharma (2019) further enhanced the selection with the Topographic Wetness Index (TWI; Beven and Kirkby, 1979) by refining the pixels to be considered downstream, which is shown to have a clearer signal to estimate streamflow (Hou et al., 2020).

Concurrently, selecting a calibration cell (with reference cells representing land brightness temperature) was also considered a key component affecting the quality of SR. Brakenridge et al. (2007) and Kugler et al. (2019) selected the calibration cell manually to satisfy certain criteria (located near the measurement cell but the least affected area by water change). Alternatively, the calibration cell can be selected automatically with $n \times n$ grid where the measurement located at the center (see Figure S1 in Supporting Information). De Groeve (2010) developed an effective automatic calibration pixel selection method, which collects a pixel presenting the 95th percentile of brightness temperature among the $n \times n$ grids neighboring the measurement pixel at each time step. In our study, this method is denoted as the C95 method, and used to calculate SR1 and SR2.

2.3 Wavelength of the signals used to construct SR

Various types of remotely sensed observations, such as active (radar) and passive (optical, infrared, and microwave) signals, all have their strengths in streamflow estimation. However, there is a well-established compromising relationship between their penetration skill and resolution as presented in Table 2: near infrared (NIR) and short-wavelength infrared (SWIR) from Moderate Resolution Imaging Spectroradiometer (MODIS), Ka-band microwave from Global Flood Detection System (GFDS), and L-band microwave from Soil Moisture and Ocean Salinity (SMOS).

Visible or infrared observations (380nm – 1mm) are affected by geophysical obstructions such as cloud, vegetation, and shadow effects, causing considerable data loss (De Groeve, 2010; Rees, 2013; Smith, 1997). These signals are more vulnerable for specific areas, such as tropical climate regions where cloud obstructions can be more persistent and pervasive (Kugler et al., 2019), despite their finer spatial resolutions (Van Dijk et al., 2016). Also, radar-derived altimetry has been used to predict water surface elevation (Paris et al., 2016; Tourian et al., 2017; Pham et al., 2018), but it also has limitations from vegetation scattering (Smith, 1997) and long revisit time (Hou et al., 2020).

Alternatively, passive microwave observations have a higher penetration skill than optical or infrared observations (Van Dijk et al., 2016; Kugler et al., 2019) but suffer from coarse spatial resolutions ($0.09^\circ \times 0.09^\circ$ to $0.25^\circ \times 0.25^\circ$). In SR calculations, the merged Ka-band microwave (7.5–11.1 mm) provided by GFDS has been widely used in previous studies (Brakenridge et al., 2007; Brakenridge

et al., 2012; Khan et al., 2014; Kim and Sharma, 2019; Revilla-Romero et al., 2015; Revilla-Romero et al., 2014) because of its daily revisit time and penetration skill (De Groeve, 2010). However, its spatial resolution suffers in picking calibration cells. Despite the reasonable calibration cell selection rationale (De Groeve, 2010), the uncertainty remains (see section 2.4) because the calibration cell may lie on land with different physical conditions, such as land cover, soil type, and elevation profiles, to the measurement cell.

The L-band microwave (15–30 cm) approach to SR has also been tested by Kugler et al. (2019) for catchments located in the Amazon having high vegetation density. Because of the L-band penetration capability, increased R values (0.80–0.92) are demonstrated for those catchments (see Table 1), which is an improved result compared to those using Ka-band (R values of 0.36–0.69). However, it has been noted that L-band is limited in calibration pixel selection due to its coarse resolution (~25 km) (Crow et al., 2017).

Therefore, selecting calibration pixels needs extra attention. Our study then aims to develop a better SR to use coarser signals such as the L-band microwave. The limitation in the L-band signal is resolved by addressing the uncertainty in the selection and specification of the calibration pixel.

Table 2 Remotely sensed data sources previously studied for stream-flow reconstruction. Note reflectance (r) represents the fraction of radiant energy reflected off the surface, and T_b is the brightness temperature, all thermal indicators are sensitive to the presence of water.

RS signal (Sensor/Mission)	Thermal data convertible to flood signal	Spatial Resolution	Wavelength / Frequency	Temporal Resolution	Penetration capacity	Study
Optical/NIR (MODIS)	T_b, r	~250m	~1440 nm (208–750THz)	to 16-day	Weak Strong	Tarpanelli et al., 2013 Li et al., 2019 Sahoo et al., 2020 Shi et al., 2020 Tarpanelli et al., 2020

RS signal (Sensor/ Mission)	Thermal data convert- ible to flood signal	Spatial Resolu- tion	Wavelength / Fre- quency	Temporal Resolu- tion	Penetration capacity	Study
SWIR (MODIS)	T_b, r	$^{\circ} \times$ 0.05 $^{\circ}$	– 2155nm (139–142 THz)	-day		Van Dijk et al., 2016 Hou et al., 2020
Ka-band (GFDS)	T_b	$^{\circ} \times$ 0.09 $^{\circ}$	mm (36.5 GHz)	-day		Brakenridge et al., 2012 Revilla- Romero et al., 2015 Van Dijk et al., 2016 Kim and Sharma, 2019 Kugler et al., 2019
L-band (SMOS)	T_b, r	$^{\circ} \times$ 0.25 $^{\circ}$	cm (1.4 GHz)	-day		Kugler et al., 2019

2.4 Uncertainty in the calibration pixel selection

Uncertainties arise from the assumptions for selecting the calibration pixel, especially for a coarse pixel of low-frequency passive microwaves (Kugler et al., 2019). Figure 1 shows a typical example at a catchment in northern Australia (G8140067, see section 4.1 for the details), where the signals from surrounding cells are not suitable as the calibration pixel, so the performance of SR is highly degraded. The calibration signal is meant to make a cohesive relationship between streamflow and the satellite signal at the measurement pixel. However, Figure 1 clearly shows that if the assumptions (Equations 4, 5, and 7) for the SR formulations are not well fulfilled (typically happens in microwave signals), then the land reflectance (or brightness temperature) in the measurement cell cannot be properly estimated from those of the calibration cell. A signal with a longer wavelength has more difficulty selecting an appropriate calibration cell

because the primary assumptions—homogeneity of physical temperatures and land cover among neighboring grid cells—are not valid.

While noise can be somewhat reduced by filtering out unreliable signals using hydrological and topographical constraints (Kim and Sharma, 2019), an improvement would be formulating a physically sound approach that does away with the necessity of selecting the calibration pixel altogether. This study addresses this point by eliminating the need to select the calibration pixel and accordingly provides markedly higher accuracy than has been possible to date by considering the real variability of land reflectance. This results in a paradigm shift in surrogate streamflow measurement, which enables low-frequency signals to predict water discharge.

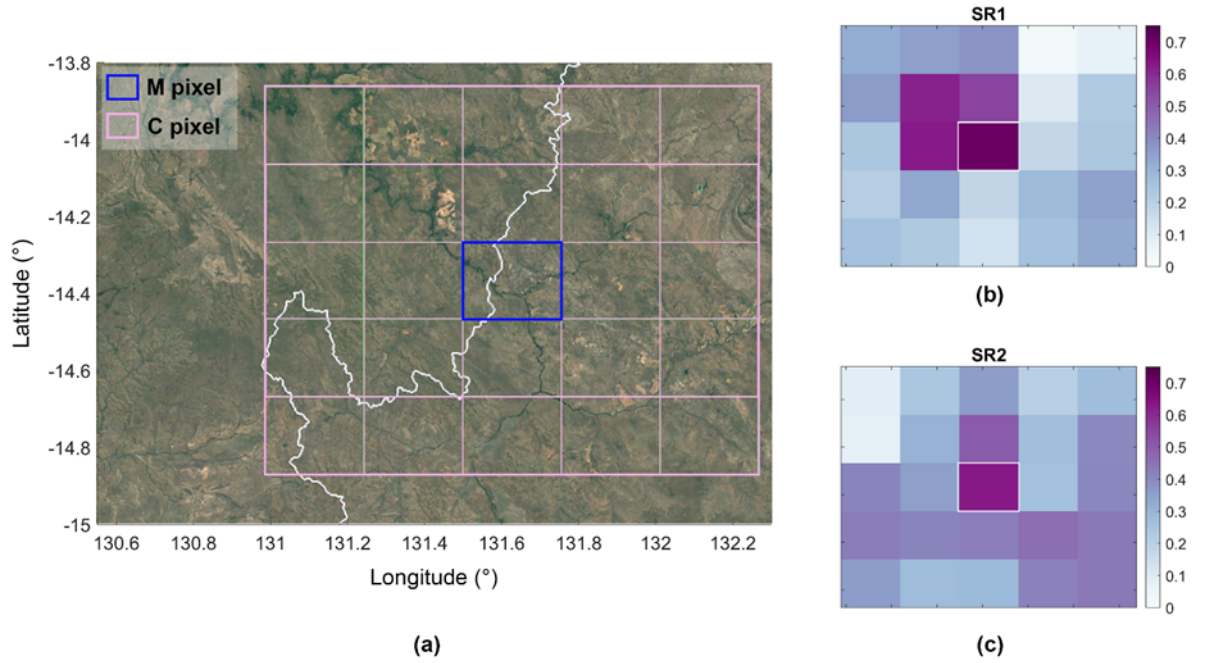


Figure 1 R of SR1 and SR2 for the catchment G8140067 for an 8-year study period (1/1/2011 to 31/12/2018). (a) The map of the catchment G8140067, where a 5×5 grid of SMOS pixels ($0.25^\circ \times 0.25^\circ$) is overlaid, and the gauge ($-14.36, 131.57$) exists at the center (blue box). The center pixel is the measurement (M) pixel, and the remaining pixels are candidates of the calibration (C) pixel (C; the set of the candidates of C pixels). (b) R values of SR1 ($T_{b,c}/T_{b,m}$) are calculated using each neighboring pixel as the calibration pixel. Here, the value on the center pixel denotes the R between Q and the time series of inversed brightness temperature ($1/T_{b,m}$) at the measure-

ment pixel, which is the baseline not using a calibration signal. (c) R values of SR2 ($\frac{r_m - r_c}{r_w - r_c}$) are calculated using each neighboring pixel as the calibration pixel. The value on the center pixel denotes the R between Q and the reflectance (r_m) of the measurement pixel. Note that none of the surrounding SR1 outperforms the baseline in terms of R. Likewise, none of the SR2 in Figure 2c surpasses their baseline, i.e., the R between Q and the time series of reflectance (r_m) at the measurement pixel. Here, the reflectance of water (r_w) is set as 0.72 with the dielectric constant 80 (Owen et al., 1961; Andryieuski et al., 2015).

3. Methodology

As analyzed in the previous section, the limitation in SR is mainly derived from two factors: 1) the need for a reference pixel and 2) the trade-off relationship between spatial resolution and penetration capability of electromagnetic waves. Although the shorter electromagnetic waves give high spatial resolution, making it easier to pick a reference pixel, it has poor penetration ability and longer revisit times. However, the longer electromagnetic waves have greater penetrative capability through the atmosphere and vegetation canopy but operate over a coarse resolution, making it hard to choose a reference pixel (Hou et al., 2020).

How then could one circumvent the use of a calibration pixel while taking advantage of the L-band microwaves' strengths to ascertain surrogate streamflow with accuracy? The solution lies in utilizing the time evolution of the measurement pixel retrievals, unlike the previous SRs using spatial references for calibration pixel selection.

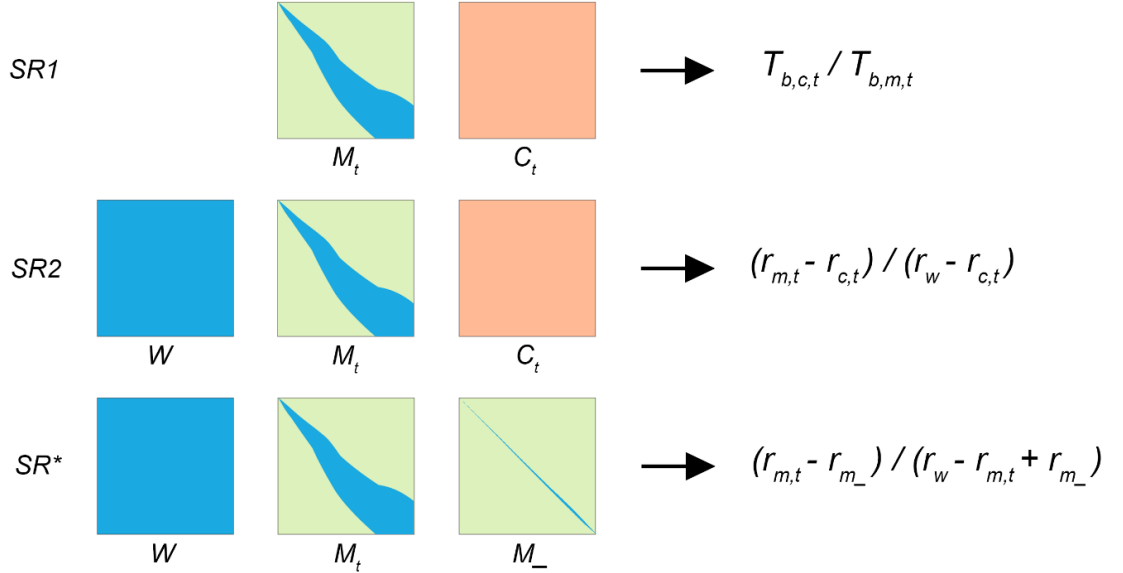


Figure 2 The concept of how SR1, SR2, and SR* are derived. SR1 compares the reflectance signals of measurement (M) and calibration (C) pixel; SR2 also considers the reflectance gap of the water and C pixel; the newly proposed SR* calculates the reflectance increment from its minimum value and the gap between the water and M pixel.

As illustrated in Figure 2, the prior SRs rely on identifying an appropriate spatial reference. For example, the initial derivation of SR (denoted here as SR1 and SR2) depends on the brightness temperature (or reflectance) of the calibration pixel (Equations 6 and 11). However, the land's heterogeneity between the calibration and measurement cells may countermine Assumption 1 (Equation 3). Therefore, unlike previous approaches, we eliminate the need for the calibration pixel in the SR formation but instead take the reference from the measurement pixel at a different point in time. The new SR (denoted as SR* hereafter) is designated as the ratio of the reflectance increased (r_m) from the driest time ($r_{m_}$, the lower baseline) and the reflectance gap ($r_w - r_m$) to the water reflectance (r_w , the upper baseline)

$$SR^* = \frac{r_m}{r_w - r_m} = \frac{r_m - r_{m_}}{r_w - r_{m_}} \cdot ()$$

Here, $r_{m_}$ can be set as the lower baseline and r_w can be set as the upper baseline in the microwave (reflectance of water > reflectance of dry land), but in shorter electromagnetic waves, such as near-infrared, it should be set inversely (reflectance of water < reflectance of dry land).

The SR* also can be derived from

$$r_m = wr_w + (1 - w)r_l \quad ()$$

which is equivalent to Equation 8. As noted in section 2.1, r_w is regarded as constant (Van Dijk et al., 2016; De Groeve, 2010). Then, a reference value is set as $r_{m_}$, the lowest recorded reflectance over the measurement time period, which should correspond to the lowest water presence w_- . Non-constant values, r_m , r_l and w , are disaggregated with their minimum value ($r_{m_}$, $r_{l_}$, and w_-) and increment at time t (r_m , r_l , and w) as,

$$r_m = r_{m_} + r_m, r_l = r_{l_} + r_l, \text{ and } w = w_- + w \quad ()$$

Then, Equation 14 is drawn by putting Equation 12 to Equation 13 as,

$$r_{m_} + r_m = (w_- + w)r_w + (1 - (w_- + w))(r_{l_} + r_l) \quad ()$$

and from this, Equation 17 is derived via Equation 16 as (see Text S1 in Supporting Information for more details),

$$r_{m_} = w_- r_w + (1 - w_-) r_{l_} \quad ()$$

$$r_m - w(r_w - r_{l_}) - (1 - (w_- + w)) r_l = 0 \quad ()$$

here, r_l is necessary to predict w , the increment of the water extent. However, only r_m is measurable, thus, an assumption is needed to solve this equation to infer w . Here an assumption is needed, such as,

$$r_l = a + b r_m + c w + \varepsilon, ()$$

and this is appropriate because r_m and r_l have analogous trend due to the soil wetness (Schmugge, 1983; Owe and Van De Griend, 1998), but may also be affected by water proportionality w . Here, a , b , c are constant values and ε is the error in this assumption. In L-band signal, $a \approx 0$, $b \approx 1$, and $c \approx 0$ can be assumed from its large grid size (this assumption is checked through Text S2, Text S3, and Figure S2 in Supporting Information). Then, the estimation of w (\widehat{w}) can be explained with r_m as

$$\widehat{w} = \frac{k_1 r_m + k_2}{(r_w - b r_m + k_3)} \propto \frac{r_m}{(r_w - r_m)} \propto \frac{r_m}{(r_w - r_m)}$$

s.t. $k_1 = 1 - b + b w_-$, $k_2 = -a(1 - w_-)$, $k_3 = c(1 - w_-) - a - r_{l-}$, $0 < b < 1$, $0 < k_1$ (19)

and detailed derivations can be found in Text S1 in Supporting Information. It should be noted that this Equation is developed for the signal which satisfies $r_l < r_m < r_w$, such as microwaves (Rees, 2013), thus, it should be derived inversely for shorter waves. Finally, the last term in Equation 19 is proportional to the \widehat{w} , therefore, it becomes the new SR (SR*) which is defined in Equation 12.

The new SR (using only a single measurement pixel) eliminates the reliance on calibration pixel selection. Instead, it applies the alternative assumption (Equation 18) to calculate SR in the absence of r_l . This new assumption is a tool for creating streamflow-correlated data and is applicable when spatial reference is unavailable. Supporting Information (Text S2, S3, and Figure S2) shows that the new assumption is more reliable in the L-band microwave than assumptions in previous approaches.

Consequently, the issue comes down to the second limitation in the previous SR—the coarse spatial scale of the L-band retrieval. However, we argue that eliminating the calibration pixel using the new logic reduces the need for finer scale retrievals. We propose that even though the new SR derivation is at a coarser resolution, the greater penetrative capability of the L-band microwave offers a better representation of actual streamflow.

4. Study Area and Data

4.1 Study Area

Our study assesses the performance of SRs for an 8-year study period (1/1/2011 to 31/12/2018) at the Australian Hydrologic Reference Stations (HRS; Zhang et al., 2016; Turner et al., 2012; Figure 4a). The 467 HRSs in total have been carefully selected and maintained by the Australian Bureau of Meteorology, representing all dominant Australian climate zones and areas which can be argued to be free from anthropogenic effects. Among the 467 HRS, the

catchment G8140067 located at Daly River is first analyzed in detail. This catchment has well-shaped features to capture the streamflow using satellite signals—specifically, it has a large catchment size of 33227km², and most of the area is covered by sparse trees (Lymburner et al., 2011). It is selected to highlight the difficulty in identifying stable calibration pixels, measuring the effects of the assumptions on the previous SRs, and comparing the dynamics of previous SRs and that of the new SR. Daily in-situ streamflow observations are used as a reference to evaluate the derived SRs. For 467 HRS across Australia, streamflow data is acquired from the Australian Bureau of Meteorology (Zhang et al., 2016; Turner et al., 2012).

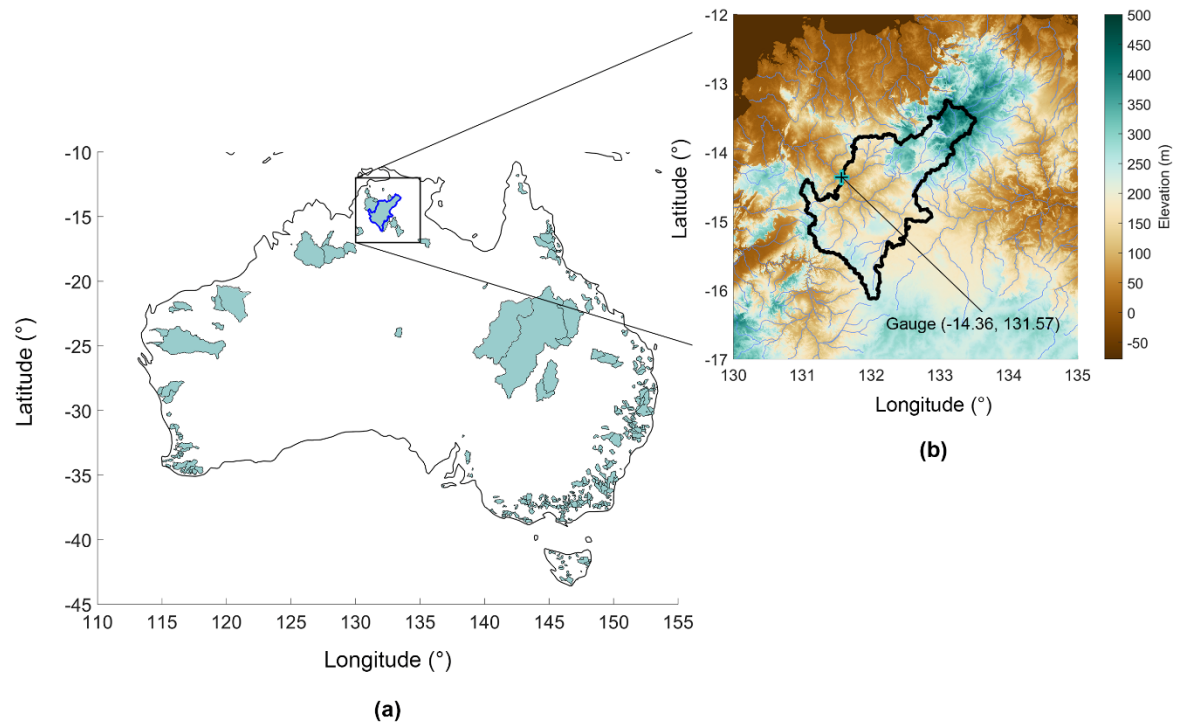


Figure 3 Study area of the study. (a) Catchment boundaries of 467 HRS catchments in Australia (colored as light blue), and one selected catchment (G8140067, blue line). (b) Magnified view of G8140067, showing elevation, catchment boundary (black line), and river streams (light blue lines).

4.2 Data

4.2.1 Microwave signals

Reflectance and brightness temperature derived from L-band microwave

Our study uses the L-band microwave to predict streamflow due to its outstanding penetrative capability over shorter waves. The signals were obtained from the French Center Aval de Traitement des Données SMOS (CATDS) ground segment of the Center National d’Etudes Spatiales (CNES) (CATDS, 2016; Al Bitar et al., 2017). SMOS daily gridded data indicated Level 3 (L3) was acquired, including brightness temperatures and dielectric constants. Because of its high sensitivity to water occurrence (Brakenridge et al., 2007), the brightness temperature in horizontal (H) polarizations was retrieved with an incidence angle of 42.5° , descending orbit variables with a $0.25^\circ \times 0.25^\circ$ resolution. Reflectance is provided via dielectric from L-MEB (Wigneron et al., 2007), and Fresnel reflection coefficient for H-polarization radiation based on Maxwell’s equations at the boundary (Rees, 2013) as

$$r = \left[\frac{\cos\theta - \sqrt{\varepsilon_r - \sin^2\theta}}{\cos\theta + \sqrt{\varepsilon_r - \sin^2\theta}} \right]^2 \quad ()$$

where ε_r is the dielectric constant, and θ is the incidence angle (42.5°).

Brightness temperature derived from Ka-band microwave

The Ka-band microwave was provided from the Global Flood Detection System (GFDS) as $0.09^\circ \times 0.09^\circ$ gridded daily brightness temperature maps at a frequency of 36.5 GHz with H-polarization. GFDS also provides one of the SR (SR1 derived from Ka-band microwave), the ratio over a wet measurement pixel with automatically selected calibration pixels (Kugler and De Groeve, 2007). By combining observations from multiple passive microwave sensors (Tropical Rainfall Measuring Mission (TRMM), Advanced Microwave Scanning Radiometer for Earth Observing System (AMSR-E), and Advanced Microwave Scanning Radiometer 2 (AMSR2)) with global coverage, the signal is enhanced by taking advantage being able to retrieve data on cloudy days.

4.2.2 Global Surface Water Data

Global Surface Water (GSW) (Pekel et al., 2016) includes statistics on the extent and change of surface water worldwide. It was produced by the European Commission Joint Research Center based on surface water mapping using 3 million images from the Landsat 5, 7, and 8 satellites during 1984–2015. GSW provides surface water occurrence, occurrence change intensity, seasonality, recurrence, transitions, and maximum water extent at a 30 m spatial resolution. Especially, the Change in Water Occurrence Intensity (CWOI) map between two epochs (16 March 1984 to 31 December 1999, and 1 January 2000 to 31 December 2020) was provided by computing the difference between the two epochs

and averaging differences between all homologous pairs of months. In our study, the CWOI clarifies the impact of changes in water occurrence at each pixel and verifies the assumptions in previous SRs and the novel SR.

5. Results

5.1 Single catchment results (G8140067)

5.1.1 Comparison of derived SR1, SR2, SR*, and streamflow

Here we validate the new approach across a diverse set of catchments. We first assess the advantages of the new SR with the selected catchment G8140067. Figure 4 shows the time series of reflectance, three derived SRs (SR1, SR2, and SR*) retrieved from L-band microwave, and in-situ streamflow (Q) from 1/1/2011 to 31/12/2018. Firstly, the 25 reflectance values of 5×5 pixels are compared (Figure 4a). In general, all the reflectance values have similar dynamics. Specifically, the reflectance values' trends do not significantly differ under wet conditions, making it hard to estimate high-flow peaks. From these dynamics of reflectance, the performance of SRs can be explained. SR1 is computed via Equation 6 using the brightness temperature. SR2 and SR* are calculated via Equations 11 and 12 using reflectance, and the reflectance of water (r_w) is set as 0.72 with the dielectric constant 80 (Owen et al., 1961; Andryieuski et al., 2015). It is shown that SR* has a high R to observed Q with a value of 0.771, while SR1 and SR2 have R values of 0.430 and 0.468, respectively. Some high-flow signals are well detected in SR1 and SR2, but there are many false high-flow signals during low-flow periods. However, SR* shows a clear alignment to streamflow Q with less noise at low-flow, indicating the improvement of SR* over SR1 or SR2.

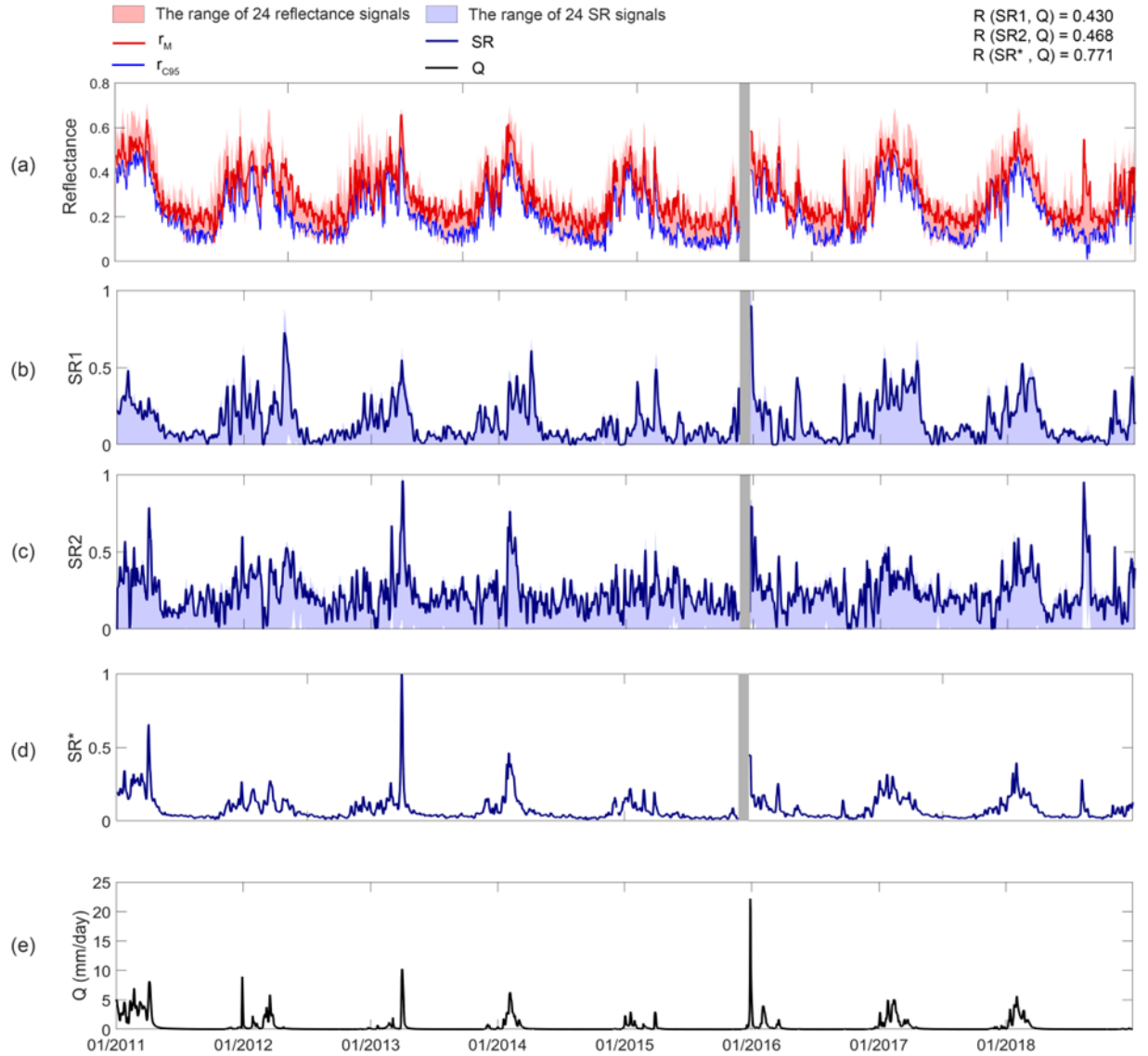


Figure 4 Full time-series of (a) reflectance, (b) SR1, (c) SR2, (d) SR*, and (e) Q of the catchment G8140067 in study period 1/1/2011 ~ 31/12/2018. There is missing data from 24/11/2015 to 24/12/2015 (vertical gray bar). (a) The range of nearby 5×5 pixels' reflectance (shaded light red) and the reflectance of M pixel (r_M ; red line) and C95 pixel (r_{C95} ; blue line) are illustrated. In (b) and (c), the range of the 24 SR signals derived from neighboring C pixels is described as a blue shade. SR_{C95} are illustrated as blue lines as a representative

value. Note that all SRs are scaled from zero to one based on the maximum and minimum values of each SR over the period for a clear comparison.

5.1.2 Validity of the assumptions in the previous form of SRs in L-band microwave

The water extent ratio in each pixel and the L-band reflectance are examined under wet and dry conditions for the study catchment. Figure 5a shows the maximum water intensity from CWOI of 5×5 pixels around the gauge of catchment G8140067, and Figure 5b and 5c show the averaged reflectance of the low-flow condition and high-flow condition. As illustrated in Figure 5c, it cannot be supposed that a grid cell that includes a water extent has higher reflectance in high-flow states. Also, from Figure 5b, it can be deduced that land reflectance is not analogous through these pixels, suggesting heterogeneity among near grid cells inferred from the reflectance under low-flow conditions. Therefore, it is not possible to substitute land reflectance (r_l) for the reflectance from the calibration pixel (r_c) in this case.

In Figure 5d and 5e, the W ratio is displayed with the distribution of reflectance in terms of pixel number, where the water extent ratio (W ratio) is calculated as the water extent area out of the measurement pixel's grid size with the water extent extracted from the maximum water occurrence from CWOI. Here no clear relationship is shown between the reflectance values and the W ratio. Specifically, Pixels 7 and 13 have high W ratios, but their reflectance values are not higher than those of other pixels. In addition, the pixels with a near-zero W ratio do not have smaller deviations of reflectance compared with other pixels, making Assumption 1 (Equation 4) inapplicable.

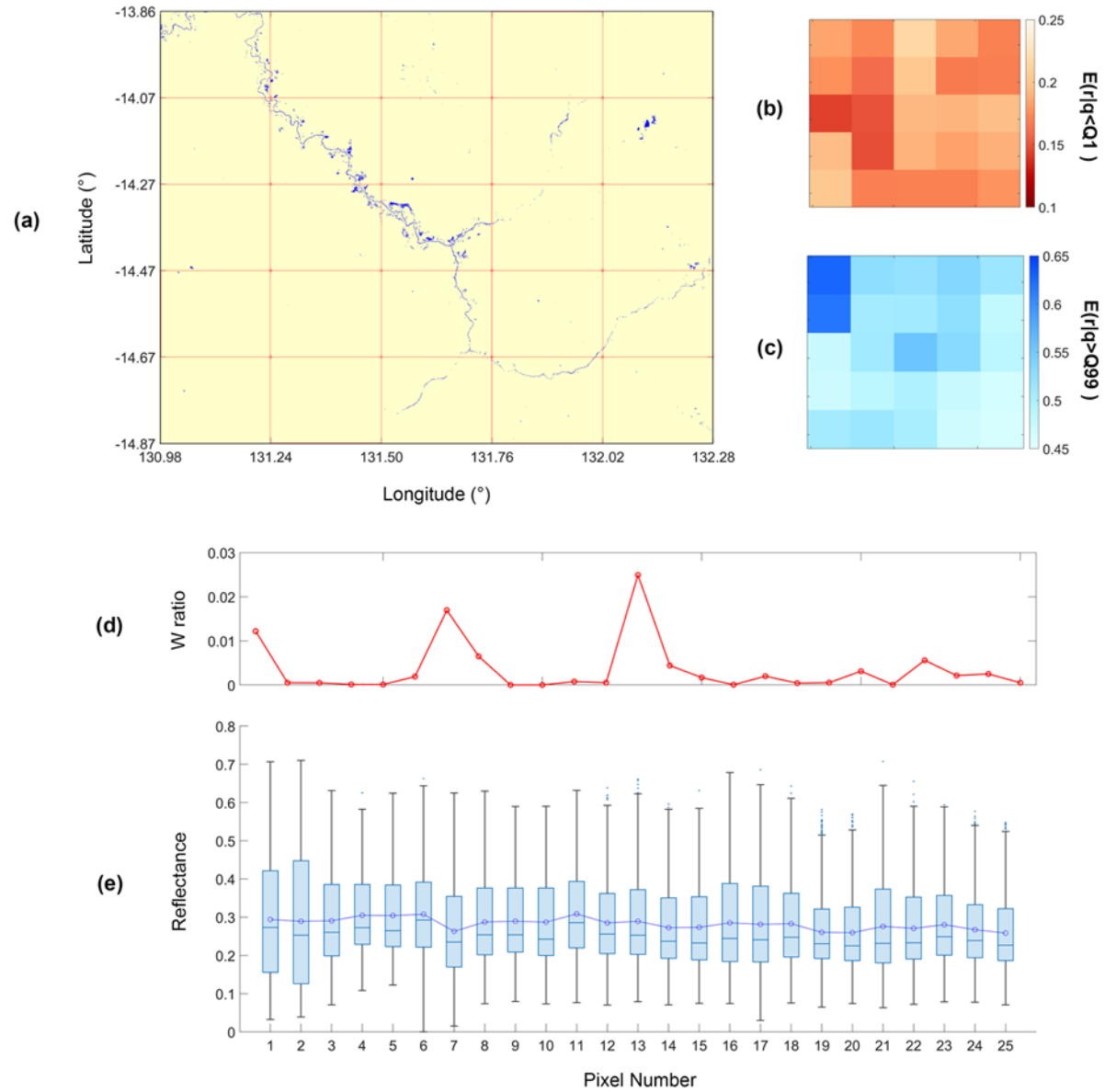


Figure 5 (a) Maximum water occurrence from GSW data. (b) The averaged value of reflectance when q is smaller than $Q1$ ($E(r|q < F_q^{-1}(0.01))$). (c) The averaged value of reflectance when q is larger than $Q99$ ($E(r|q > F_q^{-1}(0.99))$). (d) The W ratio of each pixel (e) The boxplots of reflectance of 25 pixels. The pixels are numbered as

$i = 5(m - 1) + n$ for each pixel, where n is the column number and m is the row number. The mean value of the reflectance of each pixel is described as a blue line. $F_q^{-1}(p)$ denotes the inverse function of the cumulative distribution function of streamflow (q) in terms of the probability p , which is numbered horizontally from the upper-left cell along each row

5.2 Multi-catchment analysis

5.2.1 Comparison of SR estimations

In this section, we compare the results of 467 HRS catchments to evaluate SRs in terms of two factors affecting SRs' quality: wavelength and SR formulation. Since SR1 derived with Ka-band microwave (K-SR1) has been widely studied and used as a surrogate for streamflow, as noted in section 2, it is compared to L-band products: SR1, SR2, SR* derived with L-band microwave (L-SR1, L-SR2, L-SR*, respectively).

Firstly, although there is no significant statistical difference between K-SR1 and L-SR1 in their mean R values based on a one-sided t-test (Table S1 in Supporting Information), L-SR1 exhibits advanced performance in some catchments in the Forest category (Figure 6b). This generally results from the L-band-derived signal's superior penetration capability through the vegetation canopy.

The SRs are also assessed in terms of which formulation is effective in L-band microwave. As seen in Figure 6a, L-SR1 has a mean of 0.099 (SD = 0.203), and L-SR2 has a mean of 0.189 (SD = 0.143). According to the one-sided t-test for comparing the mean values of R, L-SR2 presents higher mean values than L-SR1 (Table S1 in Supporting Information). In addition, SR1 has more negative R values, suggesting that Assumptions 2 and 3 increased overall uncertainty. The mean of R for SR* is 0.287 (SD = 0.169), showing a significant improvement over SR1 and SR2 following one-sided t-tests at significance level $\alpha = 0.05$ (Table S1 in Supporting Information).

Overall, it can be concluded that L-SR* shows considerably high performance over other signals by eliminating the calibration signal in the SR calculation (Figure 6a). Additionally, it is shown that L-SR* shows dramatically increased R values, including the area where K-SR1 could not work properly, where forest dominates (Figure 6b), and small catchments (Figure 6c) that have catchment size less than 100km².

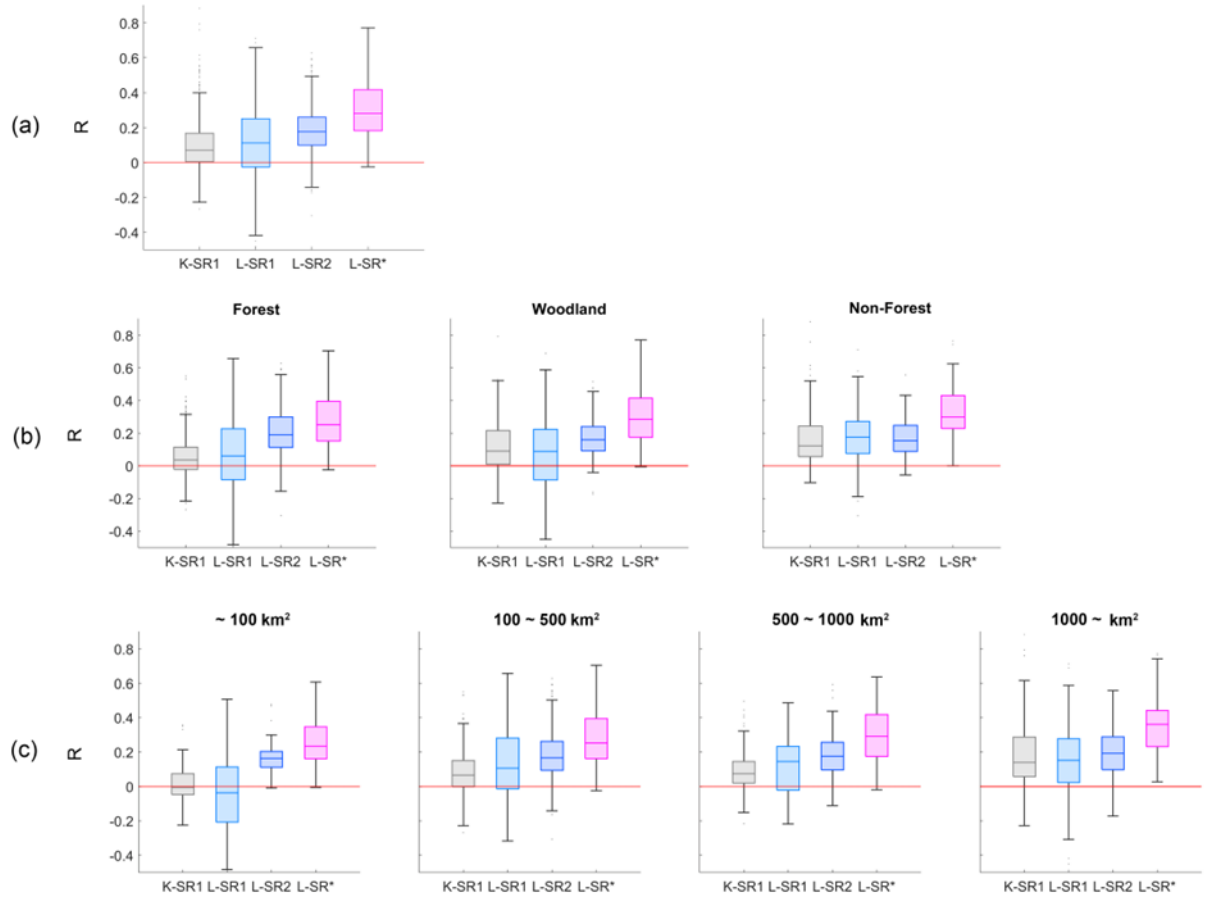


Figure 6 The distribution of R of K-SR1, L-SR1, L-SR2, and L-SR*. SR1 and SR2 are calculated with the C95 method described in section 2.1. (a) R distribution of all catchments (b) Categorized R distribution according to land type as Non-forest, Woodland forest, and Forest (ABARES (2018)) (c) Categorized R distribution according to catchment size (Zhang et al., 2016; Turner et al., 2012).

5.2.2 Improving SR with TWI filtering

Here L-SR* is further improved using the TWI filtering method (Kim and Sharma 2019). The signals from the center measurement pixel (L-SR*-CTR; the signals applied in previous figures (Figure 4 and 6)) are compared to the signals with the TWI filtering method (L-SR*-TWI) in Table 3. The performance improves when the TWI method is applied. The R for L-SR*-CTR has a mean value of 0.286 (SD = 0.169), while L-SR*-TWI shows a better result (t-test attached in Table S2 in Supporting Information) with a mean R -value

of 0.374 (SD = 0.173). Also, our final product (L-SR*-TWI) is compared to the K-SR1 enhanced with the TWI filtering method (Kim and Sharma 2019), K-SR1-TWI, the latest and the most improved system using microwave signals in previous studies in Table 3. It should also be highlighted that L-SR*-TWI has an robust performance, with 44% of catchments having an R of daily flow higher than 0.4 and 79% having an R of monthly flow higher than 0.4.

Table 3 The averaged value of the daily and monthly R and its SD, and the ratio of catchments with R exceeding specific thresholds: 0.4, 0.5, 0.6, and 0.7.

	Ka-SR1-CTR	L-SR*-CTR	Ka-SR1-TWI	L-SR* -TWI				
	Daily	Monthly	Daily	Monthly	Daily	Monthly	Daily	Monthly
Average	0.11	0.14	0.31	0.48	0.21	0.29	0.39	0.59
SD	0.16	0.26	0.16	0.22	0.15	0.26	0.17	0.20
0.4 ~ (%)	7	16	29	68	13	38	44	79
0.5 ~ (%)	3	9	14	50	5	24	26	70
0.6 ~ (%)	1	5	5	33	2	13	14	51
0.7 ~ (%)	1	3	1	16	0	5	5	34

6. Discussion

6.1 Does the new SR improve hydrologic prediction?

This study proposes a new SR methodology (denoted SR*) in providing a surrogate of streamflow that considerably outperforms the existing SR alternatives. Specifically, the new SR formulation uses a physically sounder assumption in a longer wavelength signal and eliminates the need to select the calibration pixel, enabling a ground-breaking SR performance (see Figures 4 and 6). Much of the performance degradation in the existing SRs can be attributed to noise occurring at low flows, which causes false signals, and the error that occurs when substituting $r_c(\varepsilon_c)$ with $r_l(\varepsilon_l)$. Particularly, the brightness temperature (reflectance) of the calibration pixel can be higher (lower) than that of the measurement pixel, resulting in an overestimated SR1 and SR2. This may cause a false peak SR value due to the calibration pixel’s lower reflectivity, not the increased water extent due to the higher reflectivity of the measurement pixel (Figure 4). However, eliminating the calibration allows the higher performance of L-SR* that evades the uncertainty in a calibration signal. Another improvement in the new SR is achieved by taking advantage of the L-band microwave. As shown in Figure 6, the L-band-derived SRs outperform the Ka-band ones at many HRS catchments classified as forests due to the superior penetration skill of the L-band microwave through the vegetation canopy. Moreover, it is remarkable that L-SR* shows better performance across all catchment sizes, including small catchments, showing L-SR*’s competence in small catchments.

The improvements in the new SR can be highlighted when comparing our final

result (Table 3) to those of relevant previous studies (Table 1). Also, it is promising that L-SR* will further improve model performance when it is used for hydrologic model calibration as a surrogate data of streamflow since the high correlation of SR is essential to improve inference via a hydrological model (Yoon et al., 2022).

6.2 Why does the new SR provide better predictions?

Our research also identified why the previous SR formulations are unsuitable for predicting the streamflow in the L-band microwave. Firstly, Assumption 1 (Equation 3) is the common basis for the derivation of both SR1 and SR2. This assumption’s premise is that the reflectance in low flow is similar to the calibration and measurement pixels (because the w ratio has a low impact). However, in Figure 5c, the reflectance varies in low-flow. Also, under this assumption, the reflectance values at a high-flow period should be affected by the w ratio, which means that a pixel with a higher w ratio should have a larger reflectance deviation and higher reflectance values. However, this is not found in Figures 5b, 5d, and 5e. This is mainly because of multiple geophysical factors that affect reflectance, making it difficult to set a calibration. Secondly, Assumption 3 (Equation 7) may not be valid in SR1. As seen in Figure 4, when the streamflow increases, ε_l decreases (r_l increases); thus, $1 - \varepsilon_w/\varepsilon_l$ also decreases. This also causes discord between SR1 and the streamflow. On the other hand, the assumption made in the proposed SR* is more applicable, having less errors in inferring land reflectance values (Figure S2 in Supporting Information). This makes SR more correlated to river discharge (Figure 4).

7. Conclusion

Our study aims to establish a new basis of satellite-driven SR measurement to estimate streamflow in ungauged basins. A remarkably improved SR by utilizing a longer microwave by eliminating a calibration signal. The new SR exhibits a higher correlation to streamflow, which enables a more accurate streamflow prediction. Below are the key findings of our study.

1. The new SR presents a higher correlation to streamflow than SR1 or SR2. The percentile of the HRSs that have a daily flow with $R > 0.4$ is 6.25–8.85% for SR1, 5.47–9.11% for SR2, and 28.39% for SR*, showing that selecting a proper SR dramatically impacts the data quality.
2. Our new SR approach enables the successful estimation of streamflow dynamics as the correlation of our new data (L-SR*-TWI) outweighs that of the widely studied data (Ka-SR1-TWI). Specifically, 44% of the HRSs have a daily flow of $R > 0.4$, and 79% have a monthly flow of $R > 0.4$ for L-SR*-TWI.
3. The new SR is an improvement over the previous SRs, especially in densely vegetated locations. The L-band microwave’s penetration skill advantages

in the new approach become significant by reducing the uncertainty despite the coarse spatial resolutions used.

4. We applied a new assumption that a land signal is almost identical to a measurement pixel's signal, and it is confirmed that the new assumption is physically sounder than the previous one for a long-wavelength microwave signal. Unlike the previous studies, our study focused on the temporal difference between the water body and the measurement pixel's signal, which focused on the gap between the measurement and calibration pixels' signals.
5. As our proposed SR enables runoff estimation in ungauged basins universally, it should be analyzed further worldwide. Also, the amount of streamflow can be predicted with hydrologic models specified using the proposed SR, which can yield significant benefits in simulating scenarios of future change.

Overall, this work advances the previous studies that correlated remotely sensed data to streamflow via using longer wavelength microwave signals with higher penetration skills.

Acknowledgments, Samples, and Data

This research is supported by Australian Government Research Training Program Scholarship.

Detailed access to the data: In-situ streamflow data from Australia Hydrologic Reference Stations: <http://www.bom.gov.au/water/hrs/> and <http://www.bom.gov.au/waterdata/>;

potential evapotranspiration (PET) and Rainfall data from Australian Water Availability Project (AWAP): <http://www.bom.gov.au/jsp/awap/rain/index.jsp> and <http://www.bom.gov.au/water/landscape/>;

the dielectric constant and brightness temperature from SMOS (CATDS) ground segment of the Center National d'Etudes Spatiales (CNES): <https://www.catds.fr/>;

the C/M ratio data from the GFDS: <http://www.gdacs.org/flooddetection/>;

Global Surface Water data: <https://global-surface-water.appspot.com/>;

and the DEM data from Shuttle Radar Topographic Mission (SRTM; <http://www.cgiar-csi.org/>).

References

<https://doi.org/10.12770/b57e0d3d-e6e4-4615-b2ba-6feb7166e0e6>

<https://ssrn.com/abstract=2709331><http://dx.doi.org/10.2139/ssrn.2709331>

Abares (2018). Montreal Process Implementation Group for Australia and National Forest Inventory Steering Committee, Australia's State of the Forests Re-

port 2018, ABARES, Canberra, December. CC BY 4.0. Al Bitar, A., Mialon, A., Kerr, Y. H., Cabot, F., Richaume, P., Jacquette, E., Quesney, A., Mahmoodi, A., Tarot, S., Parrens, M., Al-Yaari, A., Pellarin, T., Rodriguez-Fernandez, N. & Wigneron, J.-P. (2017). The global SMOS Level 3 daily soil moisture and brightness temperature maps. *Earth System Science Data*, 9, 293-315. Andryieuski, A., Kuznetsova, S. M., Zhukovsky, S. V., Kivshar, Y. S. & Lavrinenko, A. V. (2015). Water: Promising Opportunities For Tunable All-dielectric Electromagnetic Metamaterials. *Sci Rep*, 5, 13535. Beven, K. J. & Kirkby, M. J. (1979). A physically based, variable contributing area model of basin hydrology / Un modèle à base physique de zone d'appel variable de l'hydrologie du bassin versant. *Hydrological Sciences Bulletin*, 24, 43-69. Birkinshaw, S. J., O'donnell, G. M., Moore, P., Kilsby, C. G., Fowler, H. J. & Berry, P. a. M. (2010). Using satellite altimetry data to augment flow estimation techniques on the Mekong River. *Hydrological Processes*, 24, 3811-3825. Bjerklie, D. M., Moller, D., Smith, L. C. & Dingman, S. L. (2005). Estimating discharge in rivers using remotely sensed hydraulic information. *Journal of Hydrology*, 309, 191-209. Brakenridge, G. R., Cohen, S., Kettner, A. J., De Groeve, T., Nghiem, S. V., Syvitski, J. P. M. & Fekete, B. M. (2012). Calibration of satellite measurements of river discharge using a global hydrology model. *Journal of Hydrology*, 475, 123-136. Brakenridge, G. R., Nghiem, S. V., Anderson, E. & Chien, S. (2005). Space-based measurement of river runoff. *Eos, Transactions American Geophysical Union*, 86, 185. Brakenridge, G. R., Nghiem, S. V., Anderson, E. & Mic, R. (2007). Orbital microwave measurement of river discharge and ice status. *Water Resources Research*, 43, n/a-n/a. Brakenridge, R. & Anderson, E. (2006). MODIS-based flood detection, mapping and measurement: the potential for operational hydrological applications. In *Transboundary floods: reducing risks through flood management (pp. 1-12)*. Springer, Dordrecht. Catds (2016). CATDS-PDC L3SM Aggregated - 3-day, 10-day and monthly global map of soil moisture values from SMOS satellite. . *CATDS (CNES, IFREMER, CESBIO)*. Crow, W. T., Chen, F., Reichle, R. H. & Liu, Q. (2017). L band microwave remote sensing and land data assimilation improve the representation of prestorm soil moisture conditions for hydrologic forecasting. *Geophysical Research Letters*, 44, 5495-5503. De Groeve, T. (2010). Flood monitoring and mapping using passive microwave remote sensing in Namibia. *Geomatics, Natural Hazards and Risk*, 1, 19-35. Ghajarnia, N., Kalantari, Z., Orth, R. & Destouni, G. (2020). Close co-variation between soil moisture and runoff emerging from multi-catchment data across Europe. *Scientific Reports*, 10. Gleason, C. J., Smith, L. C. & Lee, J. (2014). Retrieval of river discharge solely from satellite imagery and at-many-stations hydraulic geometry: Sensitivity to river form and optimization parameters. *Water Resources Research*, 50, 9604-9619. Hou, J., Van Dijk, A. I. J. M. & Beck, H. E. (2020). Global satellite-based river gauging and the influence of river morphology on its application. *Remote Sensing of Environment*, 239. Khan, S., Hong, Y., Gourley, J., Khattak, M. & De Groeve, T. (2014). Multi-Sensor Imaging and Space-Ground Cross-Validation for 2010 Flood along Indus River, Pakistan. *Remote Sensing*, 6, 2393-2407. Kim, S. & Sharma, A. (2019). The Role of Floodplain Topography in Deriving Basin Discharge Using Passive Microwave

Remote Sensing. *Water Resources Research*, 55, 1707-1716.

Kugler, Z. & De Groeve, T. (2007). The Global Flood Detection System. *Office for Official Publications of the European Communities, Luxembourg*.

Kugler, Z., Nghiem, S. & Brakenridge, G. (2019). L-Band Passive Microwave Data from SMOS for River Gauging Observations in Tropical Climates. *Remote Sensing*, 11.

Li, H., Li, H., Wang, J. & Hao, X. (2019). Extending the Ability of Near-Infrared Images to Monitor Small River Discharge on the Northeastern Tibetan Plateau. *Water Resources Research*, 55, 8404-8421.

Lymburner, L., Tan, P., Mueller, N., Thackway, R., Thankappan, M., Islam, A., Lewis, A., Randall, L. & Senarath, U. (2011). The National Dynamic Land Cover Dataset - Technical report. Record 2011/031. Geoscience Australia, Canberra.

Owe, M. & Van De Griend, A. A. (1998). Comparison of soil moisture penetration depths for several bare soils at two microwave frequencies and implications for remote sensing. *Water Resources Research*, 34, 2319-2327.

Owen, B. B., Miller, R. C., Milner, C. E. & Cogan, H. L. (1961). The dielectric constant of water as a function of temperature and pressure. *The Journal of Physical Chemistry*, 11, 2065-2070.

Papa, F., Prigent, C. & Rossow, W. B. (2008). Monitoring Flood and Discharge Variations in the Large Siberian Rivers From a Multi-Satellite Technique. *Surveys in Geophysics*, 29, 297-317.

Parinussa, R. M., Lakshmi, V., Johnson, F. M. & Sharma, A. (2016). A new framework for monitoring flood inundation using readily available satellite data. *Geophysical Research Letters*, 43, 2599-2605.

Paris, A., Dias De Paiva, R., Santos Da Silva, J., Medeiros Moreira, D., Calmant, S., Garambois, P.-A., Collischonn, W., Bonnet, M.-P. & Seyler, F. (2016). Stage-discharge rating curves based on satellite altimetry and modeled discharge in the Amazon basin. *Water Resources Research*, 52, 3787-3814.

Pavelsky, T. M. (2014). Using width-based rating curves from spatially discontinuous satellite imagery to monitor river discharge. *Hydrological Processes*, n/a-n/a.

Pekel, J.-F., Cottam, A., Gorelick, N. & Belward, A. S. (2016). High-resolution mapping of global surface water and its long-term changes. *Nature*, 540, 418-422.

Pham, H. T., Marshall, L., Johnson, F. & Sharma, A. (2018). Deriving daily water levels from satellite altimetry and land surface temperature for sparsely gauged catchments: A case study for the Mekong River. *Remote Sensing of Environment*, 212, 31-46.

Rees, W. G. (2013). Physical Principles of Remote Sensing. Revilla-Romero, B., Beck, H. E., Burek, P., Salamon, P., De Roo, A. & Thielen, J. (2015). Filling the gaps: Calibrating a rainfall-runoff model using satellite-derived surface water extent. *Remote Sensing of Environment*, 171, 118-131.

Revilla-Romero, B., Thielen, J., Salamon, P., De Groeve, T. & Brakenridge, G. R. (2014). Evaluation of the satellite-based Global Flood Detection System for measuring river discharge: influence of local factors. *Hydrology and Earth System Sciences*, 18, 4467-4484.

Sahoo, D. P., Sahoo, B. & Tiwari, M. K. (2020). Copula-based probabilistic spectral algorithms for high-frequency streamflow estimation. *Remote Sensing of Environment*, 251.

Schmugge, T. J. (1983). Remote Sensing of Soil Moisture: Recent Advances. *IEEE Transactions on Geoscience and Remote Sensing*, GE-21, 336-344.

Shi, Z., Chen, Y., Liu, Q. & Huang, C. (2020). Discharge Estimation Using Harmonized Landsat and Sentinel-2 Product: Case Studies in the Murray Darling Basin. *Remote Sensing*, 12.

Smith, A., Bates,

P. D., Wing, O., Sampson, C., Quinn, N. & Neal, J. (2019). New estimates of flood exposure in developing countries using high-resolution population data. *Nature Communications*, 10.

Smith, L. C. (1997). Satellite remote sensing of river inundation area, stage, and discharge: a review. *Hydrological Processes*, 11, 1427-1439.

Smith, L. C., Isacks, B. L., Bloom, A. L. & Murray, A. B. (1996). Estimation of Discharge From Three Braided Rivers Using Synthetic Aperture Radar Satellite Imagery: Potential Application to Ungauged Basins. *Water Resources Research*, 32, 2021-2034.

Smith, L. C. & Pavelsky, T. M. (2008). Estimation of river discharge, propagation speed, and hydraulic geometry from space: Lena River, Siberia. *Water Resources Research*, 44, n/a-n/a.

Tarpanelli, A., Amarnath, G., Brocca, L., Massari, C. & Moramarco, T. (2017). Discharge estimation and forecasting by MODIS and altimetry data in Niger-Benue River. *Remote Sensing of Environment*, 195, 96-106.

Tarpanelli, A., Brocca, L., Lacava, T., Melone, F., Moramarco, T., Faruolo, M., Pergola, N. & Tramutoli, V. (2013). Toward the estimation of river discharge variations using MODIS data in ungauged basins. *Remote Sensing of Environment*, 136, 47-55.

Tarpanelli, A., Iodice, F., Brocca, L., Restano, M. & Benveniste, J. (2020). River Flow Monitoring by Sentinel-3 OLCI and MODIS: Comparison and Combination. *Remote Sensing*, 12, 3867.

Tellman, B., Sullivan, J. A., Kuhn, C., Kettner, A. J., Doyle, C. S., Brakenridge, G. R., Erickson, T. A. & Slayback, D. A. (2021). Satellite imaging reveals increased proportion of population exposed to floods. *Nature*, 596, 80-86.

Thomas, V. & López, R. (2015). Global Increase in Climate-Related Disasters (November 2015). . *Asian Development Bank Economics Working Paper Series No. 466, Available at SSRN: or* .

Tourian, M. J., Schwatke, C. & Sneeuw, N. (2017). River discharge estimation at daily resolution from satellite altimetry over an entire river basin. *Journal of Hydrology*, 546, 230-247.

Turner, M., Bari, M., Amirthanathan & G., A., Z (2012). Australian network of hydrologic reference stations-advances in design, development and implementation. *Paper Presented at the Hydrology and Water Resources Symposium 2012, Sydney, Australia*.

Van Dijk, A. I. J. M., Brakenridge, G. R., Kettner, A. J., Beck, H. E., De Groeve, T. & Schellekens, J. (2016). River gauging at global scale using optical and passive microwave remote sensing. *Water Resources Research*, 52, 6404-6418.

Vörösmarty, C. J., Willmott, C. J., Choudhury, B. J., Schloss, A. L., Stearns, T. K., Robeson, S. M. & Dorman, T. J. (1996). Analyzing the discharge regime of a large tropical river through remote sensing, ground-based climatic data, and modeling. *Water Resources Research*, 32, 3137-3150.

Wigneron, J. P., Kerr, Y., Waldteufel, P., Saleh, K., Escorihuela, M. J., Richaume, P., Ferrazzoli, P., De Rosnay, P., Gurney, R., Calvet, J. C., Grant, J. P., Guglielmetti, M., Hornbuckle, B., Mätzler, C., Pellarin, T. & Schwank, M. (2007). L-band Microwave Emission of the Biosphere (L-MEB) Model: Description and calibration against experimental data sets over crop fields. *Remote Sensing of Environment*, 107, 639-655.

Yoon, H. N., Marshall, L., Sharma, A. & Kim, S. (2022). Bayesian Model Calibration Using Surrogate Streamflow in Ungauged Catchments. *Water Resources Research*, 58.

Zhang, X. S., Amirthanathan, G. E., Bari, M. A., Laugesen, R. M., Shin, D., Kent, D. M., Macdonald, A. M., Turner, M. E. & Tuteja, N. K. (2016). How streamflow has changed across Australia since the

1950s: evidence from the network of hydrologic reference stations. *Hydrology and Earth System Sciences*, 20, 3947-3965.